

View Article Online
View Journal

# Journal of Materials Chemistry C

Materials for optical, magnetic and electronic devices

# Accepted Manuscript

This article can be cited before page numbers have been issued, to do this please use: D. Rathnaweera, X. Huai, R. Kumar, Y. Wang, J. Schlesinger, C. Bartel, S. Tewari, M. Winiarski, R. Dronskowski and T. T. Tran, *J. Mater. Chem. C*, 2025, DOI: 10.1039/D5TC02333E.



This is an Accepted Manuscript, which has been through the Royal Society of Chemistry peer review process and has been accepted for publication.

Accepted Manuscripts are published online shortly after acceptance, before technical editing, formatting and proof reading. Using this free service, authors can make their results available to the community, in citable form, before we publish the edited article. We will replace this Accepted Manuscript with the edited and formatted Advance Article as soon as it is available.

You can find more information about Accepted Manuscripts in the <u>Information for Authors</u>.

Please note that technical editing may introduce minor changes to the text and/or graphics, which may alter content. The journal's standard <u>Terms & Conditions</u> and the <u>Ethical guidelines</u> still apply. In no event shall the Royal Society of Chemistry be held responsible for any errors or omissions in this Accepted Manuscript or any consequences arising from the use of any information it contains.



# Antibonding and Electronic Instabilities in $GdRu_2X_2$ (X = Si, Ge, Sn): A New Pathway Toward Developing Centrosymmetric Skyrmion Materials

Dasuni N. Rathnaweera,<sup>1</sup> Xudong Huai,<sup>1</sup> K. Ramesh Kumar,<sup>1</sup> YiXu Wang,<sup>2</sup> Jane Schlesinger,<sup>3</sup> Christopher J. Bartel,<sup>3</sup> Sumanta Tewari,<sup>4</sup> Michał J. Winiarski,<sup>5</sup> Richard Dronskowski,<sup>2</sup> and Thao T. Tran<sup>1,\*</sup>

<sup>1</sup>Department of Chemistry, Clemson University, Clemson, South Carolina, 29634, United States.

<sup>2</sup>Chair of Solid-State and Quantum Chemistry, Institute of Inorganic Chemistry, RWTH Aachen University, 52056 Aachen, Germany.

<sup>3</sup>Department of Chemical Engineering and Materials Science, University of Minnesota, Minneapolis, Minnesota 55455, United States.

<sup>4</sup>Department of Physics, Clemson University, Clemson, South Carolina, 29634, United States.

<sup>5</sup>Faculty of Applied Physics and Mathematics and Advanced Materials Center, Gdansk University of Technology, ul. Narutowicza 11/12, 80-233 Gdansk, Poland

KEYWORDS: Magnetic skyrmion, magnetic anisotropy, RKKY exchange interactions, Fermi surface, chemical bonding, electronic instability

**ABSTRACT:** Chemical bonding is key to unlocking the potential of magnetic materials for future information technology. Magnetic skyrmions are topologically protected nano-sized spin textures that can enable high-density, low-power spin-based electronics. Despite increasing interest in the discovery of new skyrmion hosts, the electronic origins of the skyrmion formation remain unknown. Here, we study GdRu<sub>2</sub>X<sub>2</sub> (X = Si, Ge, Sn) as a model system to investigate the connection between chemical bonding, electronic instability, and the critical temperature and magnetic field at which skyrmions emerge. The nature of the electronic structure of GdRu<sub>2</sub>X<sub>2</sub> is characterized by chemical bonding, Fermi surface analysis, and the density of energy function. As X-p orbitals become more extended from Si-3p to Ge-4p and Sn-5p, improved interactions between the Gd spins and the  $[Ru_2X_2]$  conduction layer, along with increased destabilizing energy contributions, are obtained. GdRu<sub>2</sub>Si<sub>2</sub> possesses a Fermi surface nesting (FSN) vector [ $\mathbf{Q} = (q, 0, 0)$ ] r.l.u.; whereas GdRu<sub>2</sub>Ge<sub>2</sub> displays two inequivalent FSN vectors [ $\mathbf{Q}_A = (q, 0, 0)$ ;  $\mathbf{Q}_B = (q, q, 0)$ ] r.l.u., and GdRu<sub>2</sub>Sn<sub>2</sub> features multiple **Q** vectors. In addition, competing ferromagnetic and antiferromagnetic exchange interactions in the Gd plane become more pronounced as a function of X. These results reveal a correlation among the electronic instability, the strength of competing magnetic interactions, and the temperature and magnetic field conditions under which skyrmions form. This work demonstrates how chemical bonding and electronic structure can enable a new framework for understanding and developing skyrmions under desired conditions that would otherwise be impossible.

#### 1. INTRODUCTION

Understanding how chemical bonding and electronic instability influence magnetic phase transitions is crucial for developing materials for various applications, including spintronics, sensors, and quantum technologies. Skyrmions are dynamic, particle-like magnetic states capable of twisting and turning in a unique way, with sizes ranging from a few nanometers to  $\sim 100$  nm, and exhibit unique properties arising from their non-trivial topology. Their topologically protected properties provide a promising platform for studying the interaction between electronic effects and magnetic phase transitions while improving our understanding of novel states of matter. Topological protection enables skyrmions to maintain their unique properties even in the presence of defects in real materials, offering new opportunities for developing next-generation information carriers and memory architectures.  $^{19-21}$ 

Skyrmions evolution in noncentrosymmetric magnets is driven by antisymmetric Dzyaloshinskii–Moriya interactions,  $^{22-33}$  whereas skyrmions formation in centrosymmetric magnetic metals is facilitated by a delicate balance between competing exchange interactions, the Ruderman-Kittel-Kasuya-Yosida (RKKY) interactions, frustrated exchange coupling, and dipolar interactions. The long-range RKKY exchange interaction  $J(r) \sim \sin(2k_{\rm F}r) / r^3$ , where  $k_{\rm F}$  is the Fermi wavevector of conduction electrons, and r is the distance between the magnetic moments, assisted by intra-orbital magnetic frustration, promotes skyrmion formation with small sizes (a few nm).  $^{13,34-39}$ 

Gd-based centrosymmetric tetragonal lattice systems,  $GdRu_2X_2$  ( $Gd^{3+}$ , S=7/2, L=0, X=Si and Ge), have been demonstrated as skyrmion hosts with rich magnetic phase diagrams. <sup>40-44</sup> This is in part attributable to the unique crystal structure and chemical flexibility, allowing an array of atomic substitutions (**Figure 1a**). Recent theoretical studies on skyrmion hosts adopting centrosymmetric tetragonal lattices suggested several microscopic origins for skyrmion emergence, such as RKKY exchange interactions, and interorbital frustration originating in Gd-d-f spins can stabilize a spin structure with a finite modulation vector,  $\mathbf{Q}$ . <sup>45</sup> Magnetic frustration, anisotropy, high-order spin interactions and FSN have been recognized as essential physical parameters to induce phase transitions to skyrmions at a given field and temperature. <sup>46,47</sup> The elegant studies provided valuable insights into the microscopic origins of centrosymmetric skyrmion materials; however, chemical connections to critical temperature and magnetic field conditions at which skyrmions emerge remain elusive. This

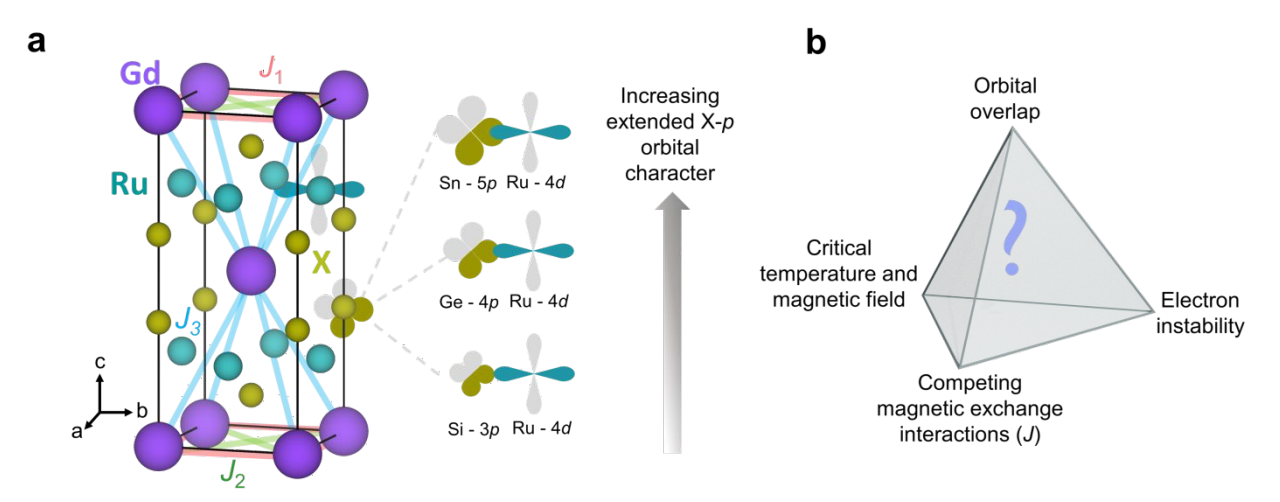


**Figure 1.** (a) Crystal structure of  $GdRu_2X_2$  (X = Si, Ge, and Sn) showing exchange interactions and increased dispersion of X-p orbitals going from Si-3p to Ge-4p and Sn-5p, and (b) Potential connections among orbital overlap, electron instability, and competing exchange interactions, and critical temperature and magnetic field conditions at which skyrmions emerge.

significantly hinders the materials development of skyrmions that may evolve at room temperature and zero field.

It has been demonstrated that in GdRu<sub>2</sub>Si<sub>2</sub>, indirect RKKY interactions stabilize equivalent magnetic modulation vectors, resulting in a square skyrmion lattice at 2 T  $\leq \mu_0 H \leq$  2.5 T, 2 K  $\leq T \leq 20$  K, with the smallest diameter of 1.9 nm among the known skyrmion materials.  $^{42,48,49}$ Magnetic torque and resistivity measurements revealed that FSN enhances the strength of the RKKY interaction, resulting in a helical modulation  $\mathbf{Q}_{A} = (0.22, 0, 0)$  r.l.u. in GdRu<sub>2</sub>Si<sub>2</sub>.<sup>42,50</sup> Angle-resolved photoelectron spectroscopy measurements in conjunction with density functional theory calculations revealed a nested Fermi surface (FS) band at the corner of the Brillouin zone that is responsible for the skyrmion formation in the Si material. <sup>51</sup> GdRu<sub>2</sub>Ge<sub>2</sub>—an isostructural compound—has recently been realized to feature the successive formation of two distinct skyrmion pockets. 40,41 Resonant X-ray scattering and magnetotransport studies suggested the presence of competing RKKY exchange interactions at inequivalent wavevectors,  $[\mathbf{Q}_A = (q, 0, 0) \text{ r.l.u.}]$  and  $\mathbf{Q}_B = (q/2, q/2, 0) \text{ r.l.u.}]$  that drive such rich topological phase formation. 40 Our previous studies have demonstrated the evolution of two skyrmion pockets in GdRu<sub>2</sub>Ge<sub>2</sub> at 2 K  $\leq$   $T \leq$  30 K, 0.9 T  $\leq \mu_0 H \leq$  1.2 T and 1.3 T  $\leq \mu_0 H \leq$  1.7 T. It is worth noting that the skyrmions in GdRu<sub>2</sub>Ge<sub>2</sub> form at higher temperatures and lower fields than those in GdRu<sub>2</sub>Si<sub>2</sub>. Electronic structure and exchange interaction evaluations revealed that the more extended Ge-4p orbitals, compared to Si-3p, enhance competing exchange interactions, thereby making the phase transition to skyrmions more accessible in GdRu<sub>2</sub>Ge<sub>2</sub> (at higher temperatures and lower fields).<sup>41</sup>

Open Access Article. Published on 22 Oktoba 2025. Downloaded on 17/11/2025 22:02:13.

bonding manifest the temperature and magnetic field conditions for skyrmion evolution in the isostructural model system  $GdRu_2X_2$  (X = Si, Ge, and Sn). While the Sn compound has not been experimentally realized due to its thermodynamically unfavorable formation energy (**Figure S1a and S1b**), its hypothesized crystal structure is optimized for this study using variable cell calculations. Our research goal is to provide some answers to the central scientific questions: What underlying chemical and electronic parameters influence the formation of skyrmions in GdRu<sub>2</sub>X<sub>2</sub>? How do they manifest in critical temperature and magnetic field conditions at which skyrmions emerge? (Figure 1b). In this study, we employ density functional theory (DFT) calculations to investigate chemical bonding via crystal orbital Hamilton population (COHP) and crystal orbital bond index (COBI), analyze Fermi surface nesting, probe electronic instability through the density of energy (DOE), and use total-energy methods to elucidate the exchange interactions in the model system. This approach enables us to delve into the impact of Si-3p/Ge-4p/Sn-5p on the orbital overlap and electronic structure of GdRu<sub>2</sub>X<sub>2</sub> and connect the chemical bonding concepts to skyrmions formation.

# 2. Computational Details

# 2.1 Quantum Espresso DFT Calculations.

The spin-polarized electronic structure, density of states, and Fermi surface calculations were performed using the Quantum ESPRESSO (QE) package. A kinetic energy cutoff of 60 Ry for the plane-wave basis set and 452 Ry for the charge density was used. The interaction between core and valence electrons was described using the projector augmented-wave (PAW) method, and the exchange-correlation functional was treated within the Perdew-Burke-Ernzerhof (PBE) formulation. For Gd, the valence configuration included  $4f^7$ ,  $5d^1$ , 6  $s^2$  with semicore  $5s^2$ ,  $5p^6$ . For Ru, the valence configuration consisted of  $4d^7$ ,  $5s^1$  with semicore  $4s^2$ ,  $4p^6$ . For Ge, the valence configuration included  $4s^2$ ,  $4p^2$ , and semicore  $3d^{10}$ . The on-site Coulomb interaction (Hubbard parameter) and Hund's exchange parameter for the Gd-4f level were set to be U = 6.7 eV and J = 0.7 eV. The double-counting correction was handled by the Fully Localized Limit (FLL) double-counting scheme, as implemented in QE. The Brillouin zone integrations were performed using a  $13 \times 13 \times 6$  Monkhorst-Pack kpoint mesh to achieve self-consistency of energy threshold of  $5 \times 10^{-9}$ Ry. Lattice parameters for GdRu<sub>2</sub>Sn<sub>2</sub> were estimated using variable cell calculation. The pseudo potential DFT calculations for the *I*-coupling constant used the same parameter, except the k-mesh was changed to  $3 \times 3 \times 2$  to account for the (2a, 2b, c) super cell. The charge and spin density maps are calculated with the pp.x in the QE package and visualized with the VESTA software. The pseudopotential wavefunctions calculated from the QE package are projected into a linear combination of atomic orbitals (LCAO) based representation by means of the Local Orbital Basis Suite Towards Electronic-Structure Reconstruction (LOBSTER)<sup>52</sup> program to extract the projected COHP (pCOHP)<sup>53</sup>, k-space COHP<sup>54</sup>, COBI<sup>55</sup>, DOE<sup>56</sup> and the molecular orbital diagrams. k-space COHP data were visualized using the functionalities implemented within the LOPOSTER code.<sup>57</sup>

Additional SCF calculations were performed to compute the Lindhard response function (LRF). To extract the Fermi surface, the self-consistent field (SCF) calculation was performed using a denser Monkhorst-Pack (MP) k-point grid. The Brillouin zone was numerically integrated for the total energy estimation using a  $38 \times 38 \times 19$  MP k-point sampling. The Fermi velocity across the Brillouin zone was mapped onto the Fermi surface as a color plot. The orbital character of the Fermi surface was computed using the Fermi projector operator, which calculates the following quantity:  $\sum_{i=1}^{n_s} \left| \left\langle \emptyset_{n_s(i)}^{atom} \mid \emptyset_{nk} \right\rangle \right|^2$  where  $n_s$  represents the number of target wavefunctions. The results from this Fermi projection calculation are saved in a format compatible with the FermiSurfer 2.4.0 software for visualization.

#### 2.2 Green's function-based DFT calculations

To estimate the magnetic exchange constants  $(I_{ii})$ , the Dzyaloshinskii–Moriya interactions (  $D_{ii}$ ), and the magnetocrystalline anisotropy constant (K), we employed the Green's function and multiple scattering theory based DFT calculation using the spin-polarized relativistic Korringa-Kohn-Rostoker (SPR-KKR) code.<sup>59</sup> The exchange-correlation potential was treated within the local density approximation (LDA) using the Vosko-Wilk-Nusair (VWN) parameterization.<sup>60</sup> Self-consistent field (SCF) calculations were carried out using the spinpolarized scalar-relativistic (SP-SREL) Dirac Hamiltonian. To achieve self-consistency, the Brillouin zone integration was carried out using a  $41 \times 41 \times 41$  k-mesh, corresponding to 68,921 k-points in the full Brillouin zone, equivalent to 4,851 irreducible k-points. The SCF mixing parameter, energy convergence tolerance and the angular momentum cutoff were set to 0.2, 0.01 mRy, respectively. The above SCF conditions successfully converged the potential, and all subsequent post-processing calculations were carried out using this converged potential. Magnetic exchange constants  $J_{ij}$  were computed within the magnetic force theorem using the Liechtenstein-Katsnelson-Antropov-Gubanov (LKAG) scheme.<sup>61</sup> Real-space couplings were evaluated up to a cluster radius  $R_c = 7.0$  and the reciprocal space coupling constant I(q) were obtained by performing a lattice Fourier transform. For estimating the Dzyaloshinskii-Moriya interactions  $(D_{ij})$  and the magnetocrystalline anisotropy energy (MAE), we carried out fully relativistic (REL) calculations using the same SCF parameters as in the scalar-relativistic calculations.

#### 3. RESULTS AND DISCUSSION

#### 3.1 Electronic Structure

We have previously studied the skyrmion host GdRu<sub>2</sub>Ge<sub>2</sub>, which adopts ThCr<sub>2</sub>Si<sub>2</sub>-type structure—a centrosymmetric tetragonal space group *I*4/mmm.<sup>41</sup> For the magnetoentropy

mapping, electrical transport and heat capacity data of the Ge material, the reader is invited to visit the reference. 41 The previous results lay some groundwork for our systematic studies on the isostructural centrosymmetric magnets  $GdRu_2X_2$  (X = Si, Ge, and Sn), of which the structure includes the Gd square lattice connected to  $[Ru_2X_2]$  layers (**Figure 1a**). To gain insight into how the electronic structure of GdRu<sub>2</sub>X<sub>2</sub> determines its physical properties, pseudo-potential spin-polarized DFT calculations were performed using the QE software package.<sup>62</sup> The crystal structure information of GdRu<sub>2</sub>X<sub>2</sub> used in the DFT computations is provided in Table S1. The band structure and density of states (DOS) results clearly demonstrate some common electronic features in GdRu<sub>2</sub>X<sub>2</sub> (**Figure 2**). The spins of the Gd-4f states are polarized, which then polarizes the Ru-4d and X-p states. The contribution of Gd-4f states is localized, deep in low energy  $\sim$  -8 eV for majority spins, and slightly above the Fermi level  $(E_F)$  energy  $\sim 4$  eV for minority spins. The spin-polarized band structure and density of states of  $GdRu_2X_2$  display a metallic behavior, where multiple bands cross  $E_F$  and finite DOS at  $E_F$ . These features demonstrate that interactions between the localized Gd-4f magnetic moments are mediated by itinerant electrons through RKKY interactions. Around  $E_F$ , the bands are mostly comprised of the Gd-5d, Ru-4d, and X-p states. The band structures exhibit an increase in overall band dispersion as the valence electron configurations progress from Si-3p, Ge-4p, and Sn-5p. This distinction becomes clearer when examining the derivatives dE/dk and  $d^2E/dk^2$  of the bands that are crossing the Fermi level. Among the 5 bands, particularly in Band-2 near the Z point, Si bands display a sudden change in slope, which gives the appearance of an abrupt dispersion change (Figure S10). By contrast, the corresponding bands for Ge and Sn evolve more smoothly and exhibit nearly parabolic dispersion, indicating more dispersive features. As a result, the extended X-p orbital character generates more diffuse features in Gd-d and Ru-d orbitals, improving the interaction between Gd-X and Ru-X (Figure 2).

# 3.2 Chemical Bonding Analysis

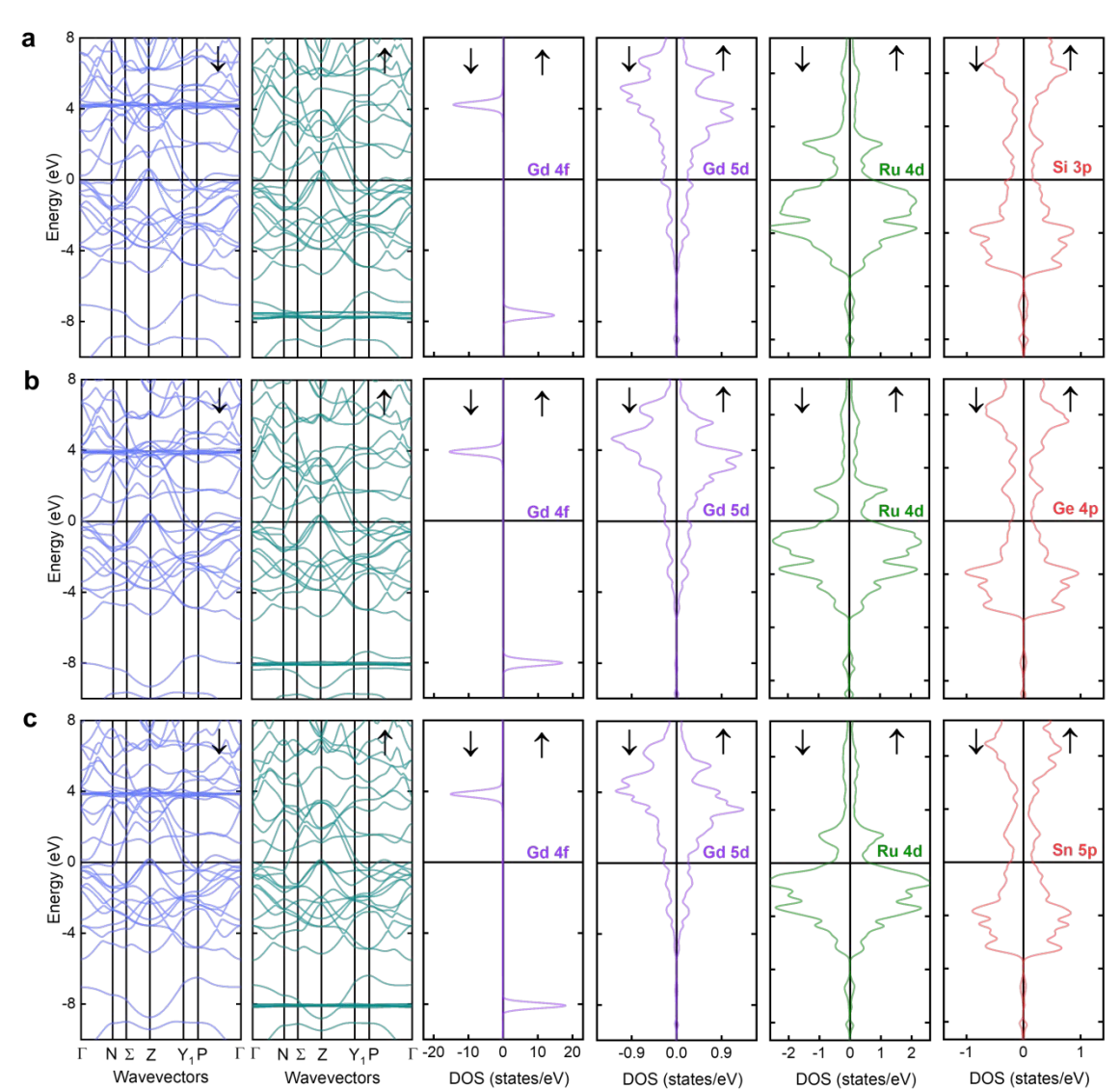


**Figure 2**. Spin-polarized band structures showing bands around the Fermi level and spin-polarized DOS of (a) GdRu<sub>2</sub>Si<sub>2</sub>, (b) GdRu<sub>2</sub>Ge<sub>2</sub>, and (c) GdRu<sub>2</sub>Sn<sub>2</sub>.

DOS analysis is helpful in describing the atom projected state contribution; however, it does not capture the phase relationships among the orbitals involved in the overlapping wavefunctions. To extract the information on bonding characters (bonding = constructive interference of wavefunctions, nonbonding = zero interference, and antibonding = destructive interference) and how the microscopic mechanisms can influence skyrmion formation, we used the Local Orbital Basis Suite Towards Electronic-Structure Reconstruction (LOBSTER) program to reconstruct the local-orbital picture from PAW wavefunctions.<sup>63-67</sup>

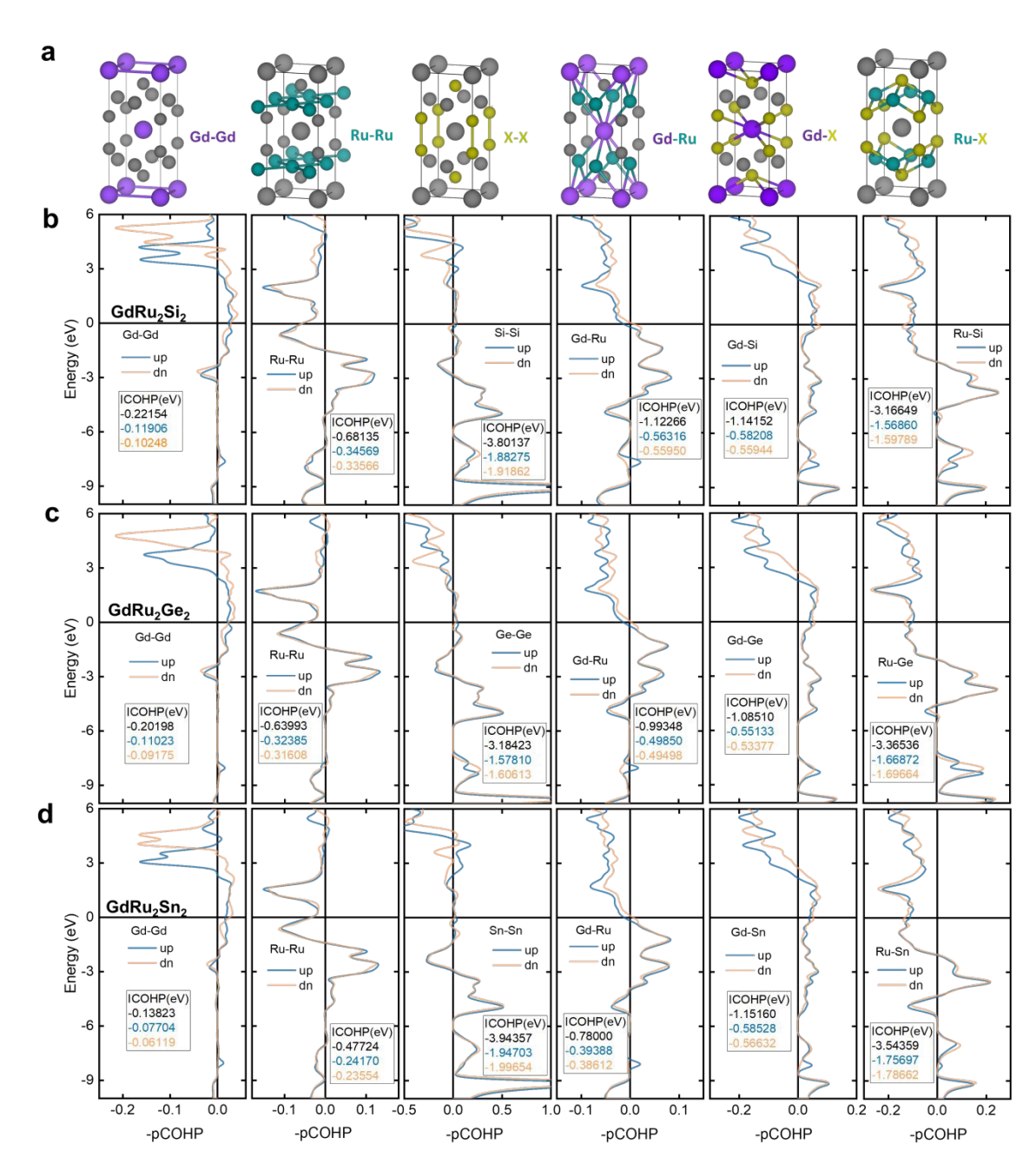


**Figure 3.** Projected crystal orbital Hamilton population (-pCOHP) curves for (a) relevant bonding environments, (b) GdRu<sub>2</sub>Si<sub>2</sub>, (c) GdRu<sub>2</sub>Ge<sub>2</sub>, and (d) GdRu<sub>2</sub>Sn<sub>2</sub> with their integrated values (ICOHP).

Crystal orbital Hamilton population (COHP) determines the energy-resolved bonding, antibonding, or nonbonding contributions between interatomic (pair-wise) interactions; whereas integrated COHP (ICOHP) estimates the overall strength of a chemical bond. The projected COHP (pCOHP) curves (**Figure 3**) indicate bonding character (-pCOHP > 0) for Gd–Gd, Gd–X, and X–X bonds and antibonding character (-pCOHP < 0) for Ru–Ru and Ru–X bonds around  $E_F$ . The integrated COHP (ICOHP) value of Gd–Gd decreases as X changes from Si to

Open Access Article. Published on 22 Oktoba 2025. Downloaded on 17/11/2025 22:02:13.

PY-NC This article is licensed under a Creative Commons Attribution-NonCommercial 3.0 Unported Licence.

Ge and Sn, suggesting a reduced overlap of the Gd orbitals. For the  $[Ru_2X_2]$  conduction layer, the increased ICOHP value of Ru-X implies an improved overlap of the Ru-d and X-p orbitals as X changes from Si to Ge and Sn. These combined features provide some insight into the improved interaction between the Gd-4f localized electrons and the  $[Ru_2X_2]$  layer as X changes from Si to Ge and Sn.

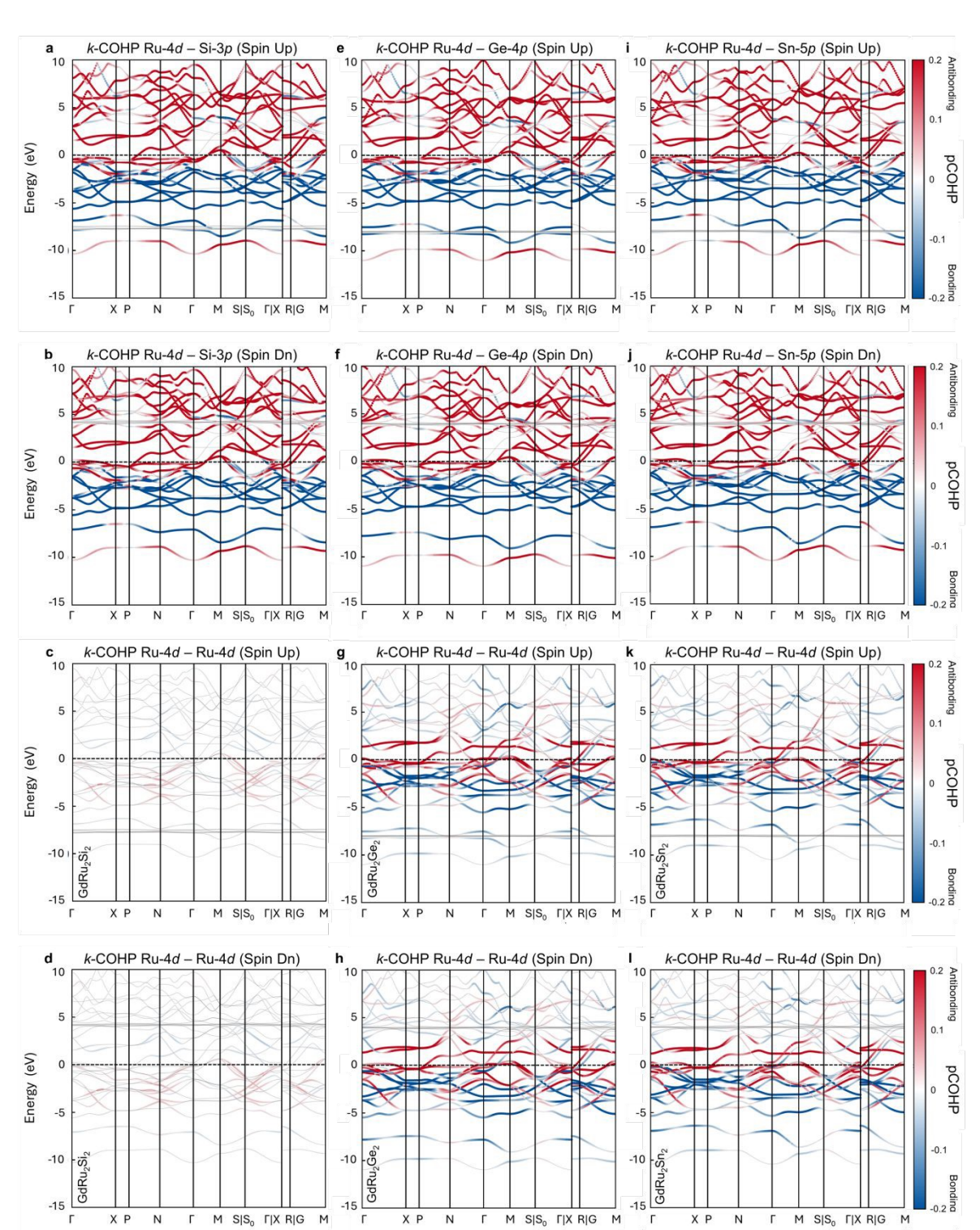


**Figure 4.** k-resolved COHP of Ru–X and Ru–Ru near  $E_F$  along the Γ–X–P–N–Γ–M path for (a-d) GdRu<sub>2</sub>Si<sub>2</sub>, (e-h) GdRu<sub>2</sub>Ge<sub>2</sub>, (i-l) GdRu<sub>2</sub>Sn<sub>2</sub>. The color scale represents pCOHP (eV).

Crystal orbital bond index (COBI) provides a generalized bond index term for crystalline solids. To quantitatively analyze the quantum-chemical bond order in solids, integrated COBI (ICOBI)<sup>55,68</sup> was calculated for all bonds (**Figure S3**). Ru–X and X–X bonds have the greatest

Open Access Article. Published on 22 Oktoba 2025. Downloaded on 17/11/2025 22:02:13.

ICOBI values of  $\sim$ 0.5, about half a bond, indicating a strong covalent bonding character. The small ICOBI value of Gd-Gd ( $\sim$ 0.03) implies negligible pairwise interactions. Overall, the COBI results are in line with and complementary to COHP.

To gain more insight into the anti-bonding occupation around the  $E_{\rm F}$ , we calculated the k-resolved COHP for Ru-4d and X-p bonds in GdRu<sub>2</sub>X<sub>2</sub>, since these orbitals are the main composition of the  $E_{\rm F}$ .<sup>69</sup> The k-COHP maps (**Figure 4**) reveal that the bonding sign switches to antibonding well below  $E_{\rm F}$  and then persists up to and across  $E_{\rm F}$ , with a continuous antibonding range from roughly –1.2 eV to 0 eV, for both Ru–X and Ru–Ru pairs. Moving from Si to Ge and Sn, the Ru–X antibonding strengthens modestly (**Figure 4**, first two rows), whereas the Ru–Ru antibonding grows substantially (**Figure 4**, last two rows), indicating that the common Ru sublattice experiences progressively stronger destabilization around  $E_{\rm F}$  as a function of X. We attribute this trend to strong bonding among [Ru<sub>2</sub>X<sub>2</sub>] slab (seen in the COHP) that enhances Ru–X mixing and, in turn, feeds the Ru–Ru antibonding near  $E_{\rm F}$ . Spinresolved panels show nearly comparable contributions from the majority and minority spins, with the minority spin channel lying slightly closer to  $E_{\rm F}$ ; thus, the effect is not strongly spin-selective in this collinear setting.

Crucially, the strongest, flat, antibonding segments near  $E_{\rm F}$  cluster along  $\Gamma$ -X and P-N in the  $-1.2~{\rm eV}-0~{\rm eV}$  energy window, while X-P also appears antibonding but sits relatively farther from  $E_{\rm F}$  (**Figure 4**). This directional pattern matters: the  $\Gamma$ -X and P-N segments identify the k-space regions most capable of low-energy scattering, providing a bond-specific map of where the electronic structure is primed for modulation. Along P-N, the k-COHP plot shows a progressive shift of antibonding bands toward  $E_{\rm F}$ : it remains below  $E_{\rm F}$  in Si, approaches  $E_{\rm F}$  in Ge, and crosses  $E_{\rm F}$  in Sn. Together with the flat, near-  $E_{\rm F}$  antibonding seen along  $\Gamma$ -X, these features delineate specific k-space segments where low-energy scattering is available. While a full analysis is presented later, we note that this evolution could be consistent with the directions of the FSN vectors and may relate to the multi- ${\bf Q}$  behavior observed only in Ge and Sn compounds.

# 3.3 Spin Density Analysis

Spin, charge, and orbital are the three fundamental components of an electron. Next, we examine spin and charge density maps while considering orbital contributions. Spin density maps ( $\rho_{up}$  -  $\rho_{down}$ ) projected on selected lattice planes illustrate supplementary evidence for the effect of the X-p orbitals on spin polarization (**Figure 5**).<sup>70</sup> In the [100] plane cutting through Gd, Ru, and X (**Figure 5a**), the spin polarization of the [Ru<sub>2</sub>X<sub>2</sub>] layer is enhanced as X changes from Si to Ge and Sn. **Figure 5b-c** shows the [001] plane slicing through Gd and X and between Ru and X, respectively. The spin density of Gd and Ru in these projections

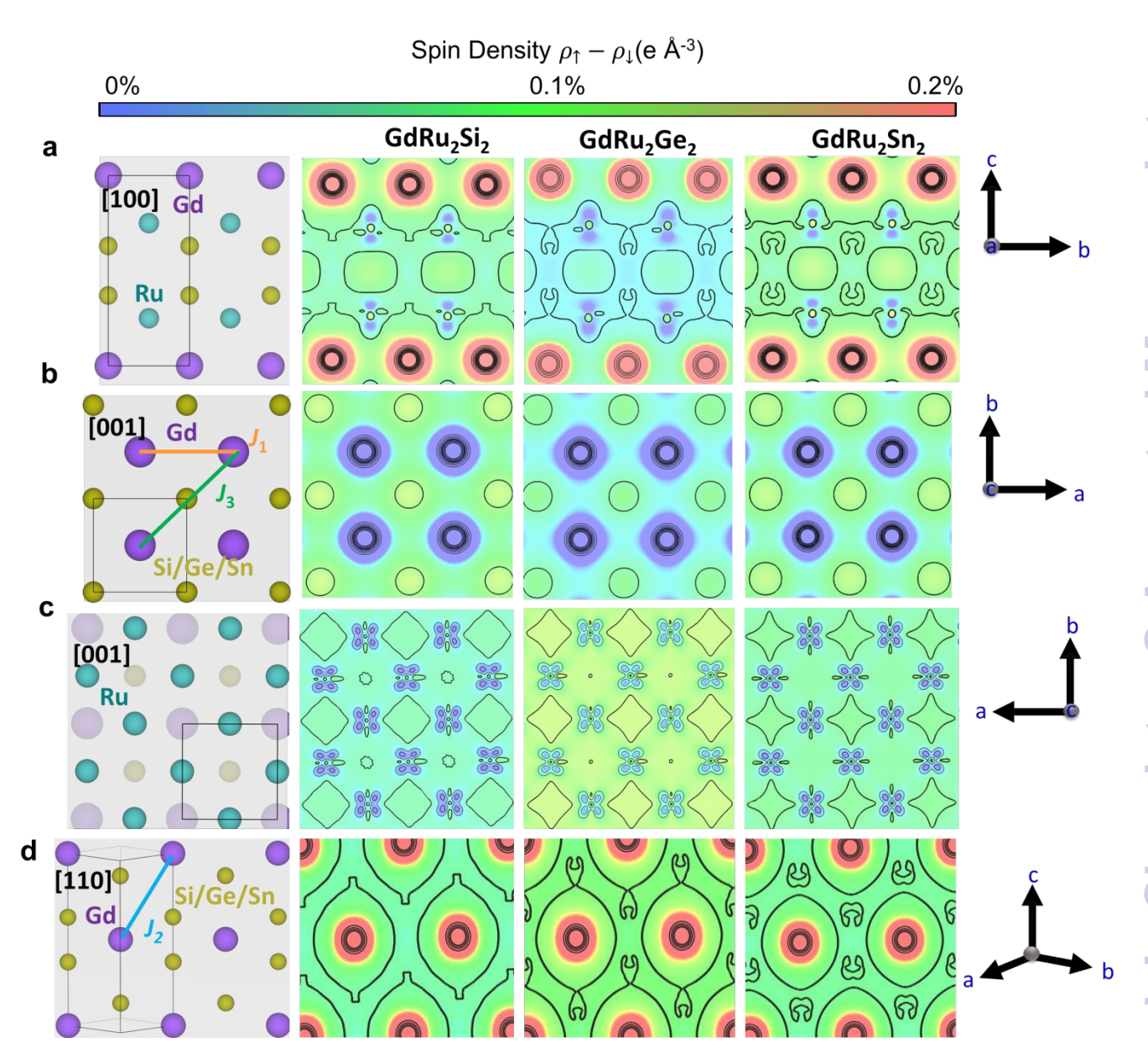


**Figure 5.** Spin density map of  $GdRu_2X_2$  (a) [100] plane cutting through Gd, Ru, and X atoms, (b) [001] plane cutting though Gd and X atoms, (c) [001] plane cutting in between Ru and Ru atoms, and (d) [110] plane cutting through Gu atoms (X= Si, Gu, and Sn). The color bar provides a qualitative indication of the relative magnitude of spin polarization.

becomes more polarized, following the trend  $GdRu_2Si_2 < GdRu_2Ge_2 < GdRu_2Sn_2$ . The tunable spin polarization as a function of X-3p/4p/5p orbitals suggests the feasibility of modifying interactions between the Gd localized magnetic spins and the  $[Ru_2X_2]$  conduction layer—ingredients for RKKY interactions. As shown in **Figure 5a-d**, the Gd site exhibits a strong, red-colored, spherically symmetric contour pattern, indicating well-localized Gd-4f magnetic moments. In the vicinity of the Gd moment, the Ru–X layer exhibits spin density in the blue-

Open Access Article. Published on 22 Oktoba 2025. Downloaded on 17/11/2025 22:02:13.

This article is licensed under a Creative Commons Attribution-NonCommercial 3.0 Unported Licence.

purple color, reflecting strong hybridization between the Ru-4d states and X-p states (**Figure 5a**). If we interpret the blue-purple region as induced spin polarization due to the RKKY interaction, it becomes evident from **Figure 5a** that the substitution of the X atom from Si to Ge to Sn leads to subtle changes in both the intensity and the spin density contours along the [100] direction. The contour lines emerging along the [100] projection indicate spin density elongation and are associated with the FSN vector  $\mathbf{Q}_{A} = (q, 0, 0)$  r.l.u. experimentally observed for  $\mathrm{GdRu_2Si_2}$  and  $\mathrm{GdRu_2Ge_2}$ . Additionally, short, wave-like modulations in the form of spin density lobes along the b-axis are observed in **Figure 5a**. The spin density wave along the a-axis (a and b are equivalent in tetragonal systems) can be linked to the experimentally

observed propagation vector  $\mathbf{Q}_{A}$  = (0.22, 0, 0) r.l.u. Furthermore, the Ge variant shows visibly stronger polarization and a tendency to diffuse along the c-axis, suggesting that the enhanced orbital spatial extension of Ge-4p and Sn-5p facilitates increased hybridization and thereby supports FSN. Another interesting feature is observed along the [110] direction in the spin density contours. For the Si system, we observe nearly isotropic spin polarization at the Gd site. In contrast, the Ge and Sn variants exhibit reconfigured spin density contours around Gd, indicating the presence of additional spin density modulations (Figure 5d). This

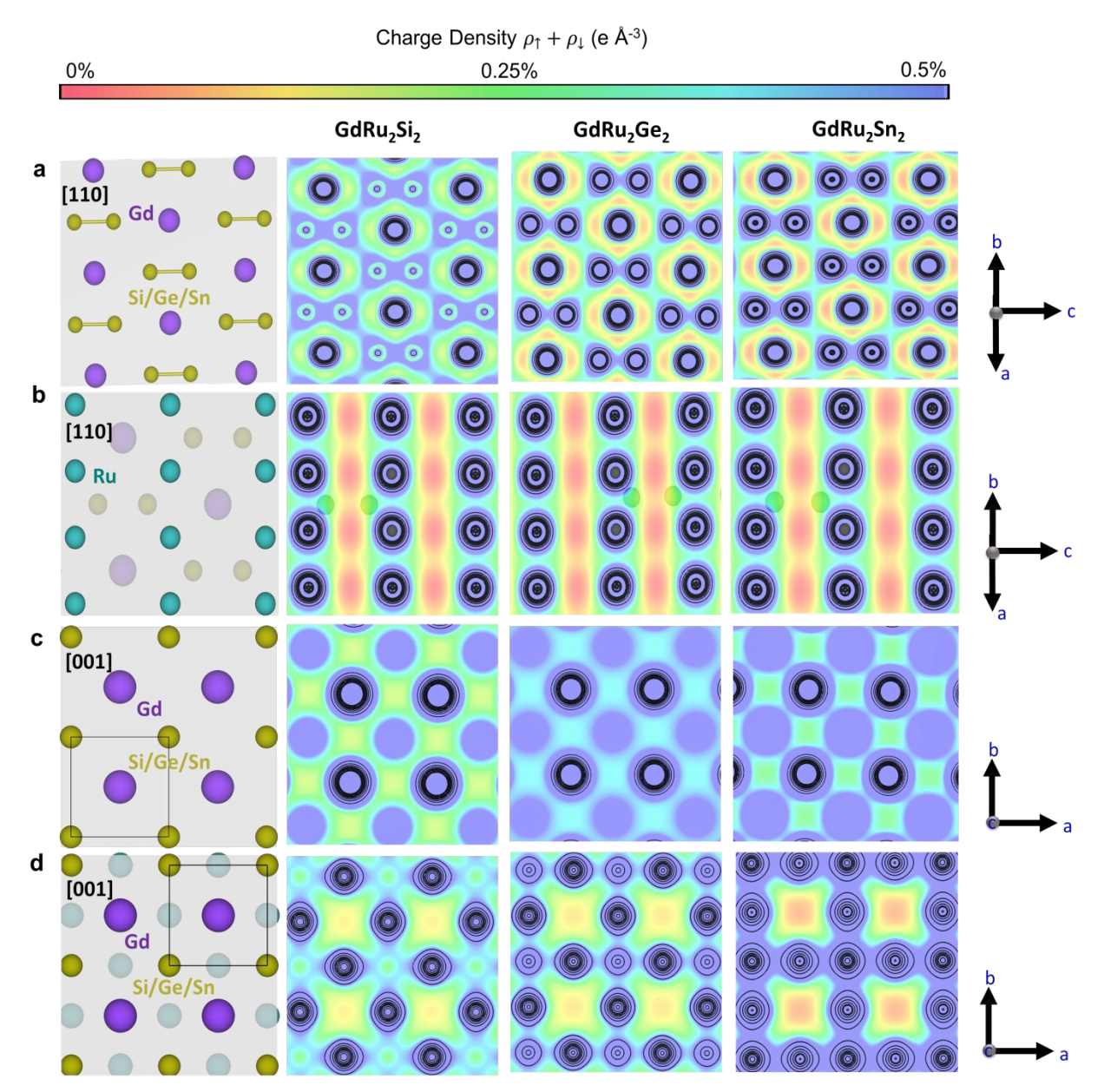


**Figure 6**. Charge density map of GdRu<sub>2</sub>X<sub>2</sub> (a) [110] plane cutting through Gd and X atoms, (b) [110] plane cutting through Ru layer, (c) [001] cutting through Gd and X atoms, and (d) [001] plane in between Ru and X atoms. (X= Si, Ge, and Sn).

Open Access Article. Published on 22 Oktoba 2025. Downloaded on 17/11/2025 22:02:13.

observation aligns with experimental reports of inequivalent multiple modulation vectors in  $GdRu_2Ge_2$ . Since we do not observe a clear antiferromagnetic-like coupling between the 4f moments and the Ru–X layer as seen in the [100] modulation, the spin density contours along [110] may originate from inter-orbital frustration between Gd-4f and Gd-5d. Similar spin density features are observed in the [110] projection (**Figure S5**), connecting to the  $\mathbf{Q}_B = (q, q, 0)$  r.l.u. FSN vector in  $GdRu_2X_2$ . A more detailed description of FSN is discussed in the subsequent sections.

### 3.4 Charge Density Analysis

In addition to the spin density, charge density maps visually represent the distribution of electronic charge within the  $GdRu_2X_2$  crystal (**Figure 6**).<sup>70</sup> **Figure 6a** highlights the [110] projection on the Gd and X planes. As X changes from Si to Ge to Sn, the charge density of the X–X dumbbells increases, enhancing the charge anisotropy of Gd. Meanwhile, **Figure 6b** shows the [110] plane cutting through the Ru layer, where the charge distribution of Gd appears more diffused. **Figures 6c** and **6d** show the [001] projections on the Gd and X plane and the plane between Ru and X, respectively. As X goes from Si to Ge and Sn, the charge density of Gd and  $[Ru_2X_2]$  increases and becomes more dispersed. This indicates improved bonding interactions between Gd and  $[Ru_2X_2]$ .

# 3.5 Electronic Instability

# 3.5.1 Fermi surface nesting and Lindhard response function

Electronic instability around  $E_F$  in metals gives rise to phase transitions to novel states of matter under external perturbations, such as temperature and field.<sup>69,70</sup> To describe how itinerant electrons behave under the influence of various interactions in  $GdRu_2X_2$ , we extracted the Fermi surface from the bands that  $cross\ E_F$ . The Fermi surface topology and potential nesting in the Si and Ge materials as well as in  $Gd_2PdSi_3$  have been realized to enable spin spiral magnetic ordering and double- $\mathbf{Q}$  density wave modulation.<sup>40,46,51,71</sup> There are situations where sections of the Fermi surface are parallel (or nearly parallel) and can be connected by a single nesting vector  $\mathbf{Q}$ , leading to instabilities such as charge and spin density waves in materials. There is a general agreement in the literature regarding the FSN driving the helical and skyrmion phases. However, minor discrepancies arise regarding the specific nesting vector. Despite several studies, the precise modulation vector and the specific portion of the FS responsible for nesting remain unresolved in  $GdRu_2X_2$  (X = Si, Ge).

To further understand FSN in  $GdRu_2X_2$  (X = Si, Ge, Sn) and whether and how the modification of X-p orbitals influences nesting vectors, we examine the FS and the LRF for  $GdRu_2X_2$ . **Figures 7** and **8** present the FS diagrams for both spin-up and spin-down channels, along

with the corresponding LRF projected along the [100] and [111] directions, respectively. Our calculations showed five distinct FSs in the Si and Ge materials, and only four FSs in the Sn variant (Figure S6), agreeing well with the band structures. The presence of small, ellipsoidal FSs at the **Z** point is common in GdRu<sub>2</sub>X<sub>2</sub> (**Figure S6**). These smaller ellipsoid pockets are identified as localized hole pockets and show parallel features at the **Z** point. However, LRF and other experimental evidence are absent for such modulation. A larger barrel-like FS (band 4 for Si/Ge and band 3 for Sn) is observed in all three compounds. This surface extends to the zone boundary and shows strong dispersion along the  $k_x$  and  $k_y$ directions with limited dispersion along the  $k_z$  direction (Figure S6). These features are observed for both spin-up and spin-down channels. Additionally, band 5 (band 4 for Sn) shows a distinct difference between spin-up and spin-down channels. We observed a less dispersive parallel surface centered at the **X** point in the spin-down channel. In contrast, the spin-up band is well extended (tubular type FS) within the Brillouin zone, suggesting significant band interaction, possibly due to the influence of 4f and 5d orbital mixing and/or multi-band effects of Ru-4d (Figure 7a, c and e). This band primarily arises from Gd-5d and Ru-4d states, crosses  $E_F$  at multiple k-points, and displays linear dispersion just below  $E_F$  and a flat band segment along the  $\mathbf{Z}$ - $\mathbf{Y}_1$ - $\mathbf{P}$ - $\mathbf{\Gamma}$  direction, indicating potential topological features (Figure 2). Overall, this analysis highlights the similarities and differences in the FS characteristics in GdRu<sub>2</sub>X<sub>2</sub>. However, these characteristics alone cannot definitively determine the presence or absence of FSN in this system. Therefore, we employed the FermiSurfer software to compute the LRF from the conventional Fermi surface.

FSN and associated divergence in electronic susceptibility, owing to lattice instability, spin density wave modulation, or Friedel oscillations, are understood in several low-dimensional systems through the Lindhard susceptibility or Lindhard Response Function (LRF).<sup>69,72-74</sup>

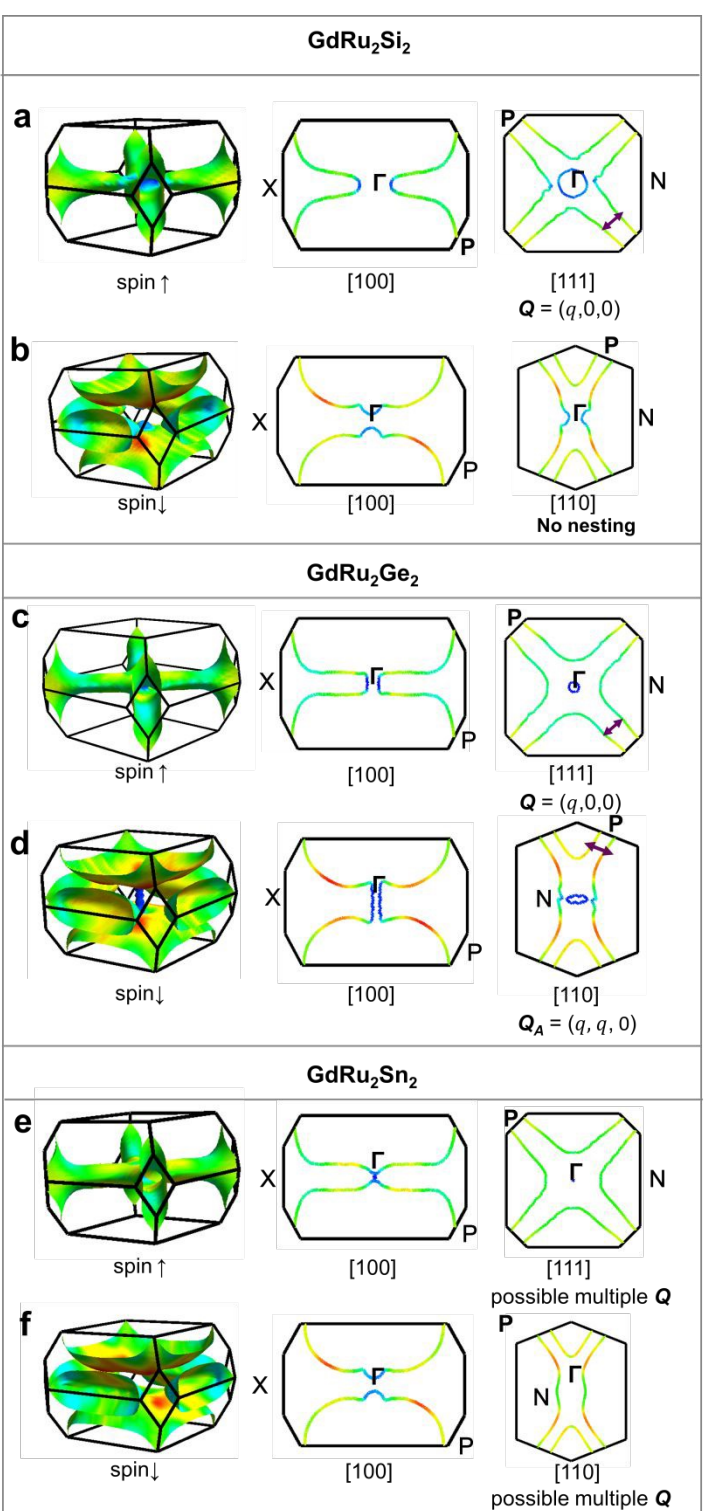


**Figure 7.** Fermi surface nesting with respective projections indicating nesting vector for (**a-b**) GdRu<sub>2</sub>Si<sub>2</sub>, (**c-d**) GdRu<sub>2</sub>Ge<sub>2</sub>, and (**e-f**) GdRu<sub>2</sub>Sn<sub>2</sub>, respectively.

Such electronic instabilities show up as part of parallel segments in FS. the However, these apparently parallel sections themselves are insufficient to draw conclusive evidence for FSN, as certain geometric and energy conditions are required to obtain FSN. One way determine a possible FSN is by calculating the Lindhard susceptibility function  $\chi'(q)$  that describes the stability of the electron system. The Lindhard susceptibility function can be written as,

$$\chi^{\prime(q)} = \sum_{k} \frac{f(\varepsilon_{k}) - f(\varepsilon_{k+q})}{\varepsilon_{k} - \varepsilon_{k+q}} \tag{1}$$

where a  $f(\varepsilon_k)$  and  $f(\varepsilon_{k+q})$  are Fermi-Dirac probability distribution functions related to the occupancy of the states with  $\varepsilon_{k+q}$  $\varepsilon_k$ energy and respectively.<sup>74</sup> The above equation assumes that the kdependent matrix element is set (unity), to a constant representing non-interacting electronic susceptibility. Such a function captures the details of the Fermi surface topology and geometrical features; however, the orbital contribution, SOC or multiband effect are captured only if we include the kdependent matrix element.

The observed parallel regions centered around the **X** point,

perpendicular to the  $\Gamma$ -X direction, suggest a nesting vector  $\mathbf{Q}_A = (q, 0, 0)$  (**Figure 7a** and **7c**), in agreement with\_previous reports.<sup>40,51</sup> There are diffuse peaks in the Lindhard function at the **X** point, which is consistent with the observation of the parallel surfaces for both spin-up and spin-down channels for all three compounds. (**Figures 7a** and **7c**). In addition, FS and LRF show potential nesting along  $\mathbf{Q}_B = (q, q, 0)$  r.l.u. and  $\mathbf{Q}_{B'} = (-q, -q, 0)$  r.l.u. for GdRu<sub>2</sub>Ge<sub>2</sub> (**Figure S7**). This multi- $\mathbf{Q}$  FSN features in GdRu<sub>2</sub>Ge<sub>2</sub> are supported by the work by Yoshimoshi et al., which suggests that the competition of RKKY interactions at inequivalent wavevectors drives the formation of such a rich topological phase.<sup>40</sup> This feature is observed only with Ge and Sn variants, whereas Si shows no nesting along these directions.

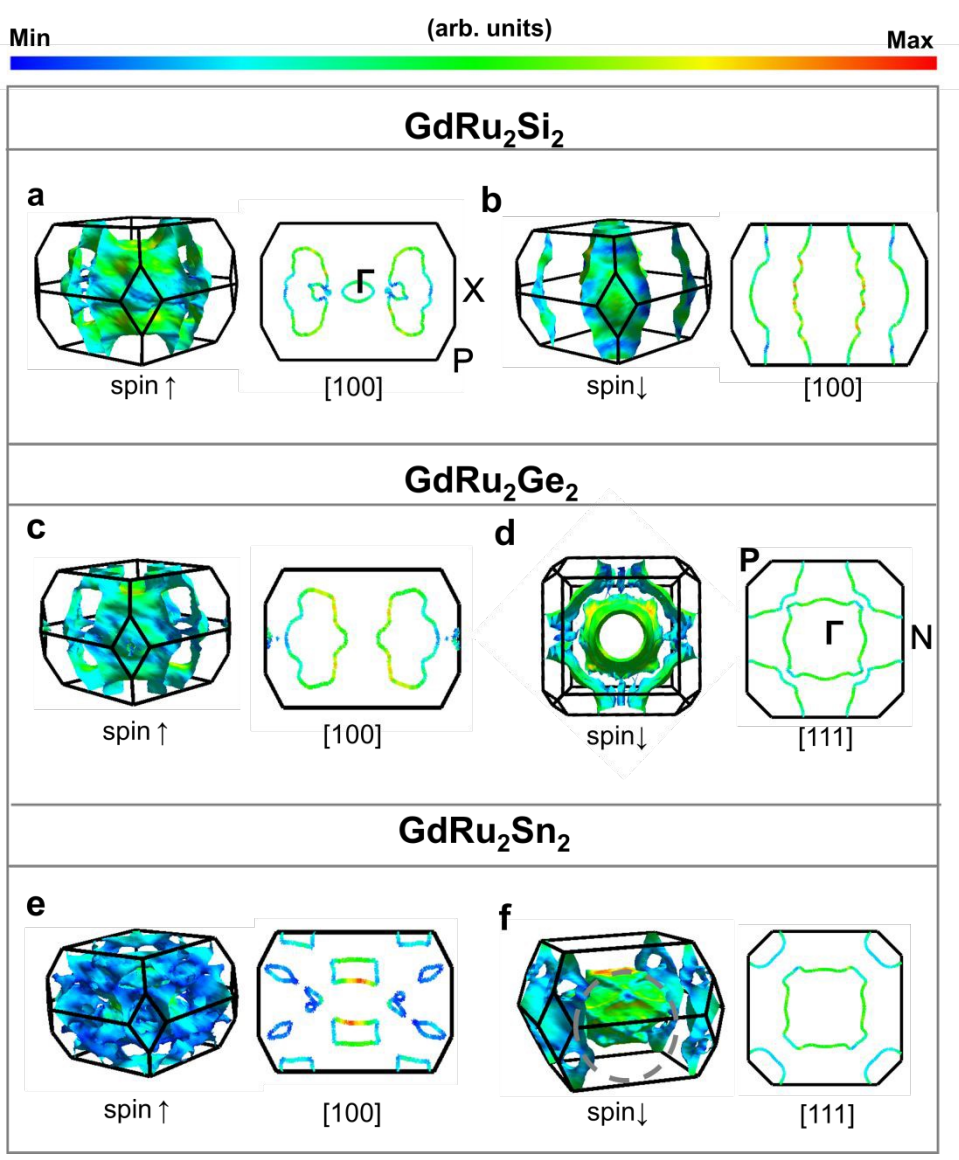


**Figure 8.** Lindhard response function with respective projections for (**a-b**)  $GdRu_2Si_2$  (**c-d**)  $GdRu_2Ge_2$ , and (**e-f**)  $GdRu_2Sn_2$  respectively. The color bar indicates the real part of  $\chi_0(q,0)$  in arbitrary units.

Open Access Article. Published on 22 Oktoba 2025. Downloaded on 17/11/2025 22:02:13.

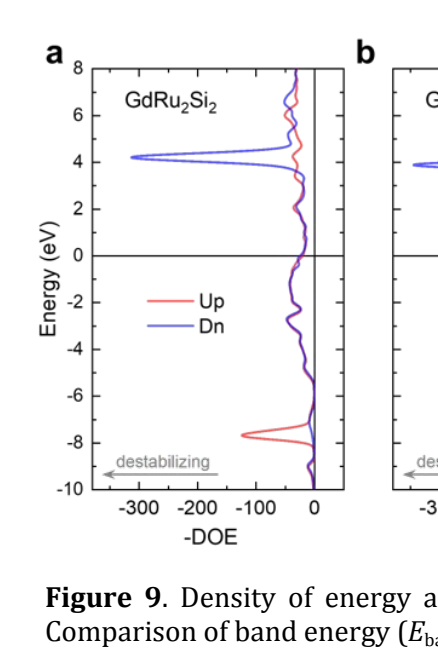
For  $GdRu_2Sn_2$ , the Lindhard susceptibility possesses diffuse features for spin-up and doubly degenerate susceptibility peaks and rhombohedral ridge patterns for spin-down (**Figure 8f**). These rhombohedral features are also observed in the spin-down channel for  $GdRu_2Ge_2$ . These complex features in the Lindhard response indicate the presence of multiple nesting wavevectors in  $GdRu_2Sn_2$ . This could be attributed to the interactions between the Gd-f/d spins and the  $[Ru_2Sn_2]$  layer, as demonstrated by chemical bonding analysis. Our FSN and LRF analysis capture the interplay between the RKKY interaction and conduction electron density modulation, which is essential for the stabilization of topologically nontrivial spin states in  $GdRu_2X_2$ . The real part of the LRF, governed by equation (1), can be used to screen geometrical features linked to potential nesting, as observed in a peak or ridge pattern corresponding to electronic instability. However, directly linking nesting to a Periels instability or density wave ordering must be done by incorporating the k-dependent matrix elements.

Consistent with these FSN assignments, as mentioned above, the k-resolved COHP identifies  $E_F$ -proximal antibonding segments along  $\Gamma$ -X and, more sensitively, along P-N, which shift toward and through  $E_F$  across the series (below  $E_F$  in Si, near  $E_F$  in Ge, and crossing  $E_F$  in Sn). These k-localized antibonding features occur precisely on the band segments that define the parallel FS sheets underlying  $\mathbf{Q}_A = (q, 0, 0)$  r.l.u and the inequivalent  $\mathbf{Q}_B = (q, q, 0)$  r.l.u directions. This observation suggests that the occupied antibonding state near  $E_F$  enhances susceptibility along those vectors and may facilitate multi- $\mathbf{Q}$  behavior in Ge and Sn, where the P-N antibonding is around or crosses  $E_F$ , respectively.

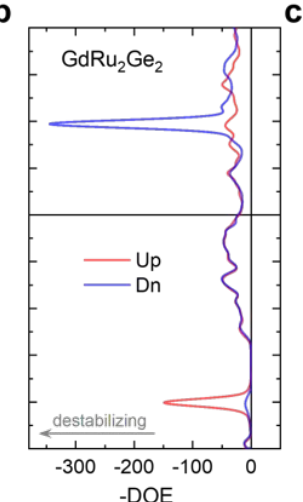
# 3.5.2 Density of Energy

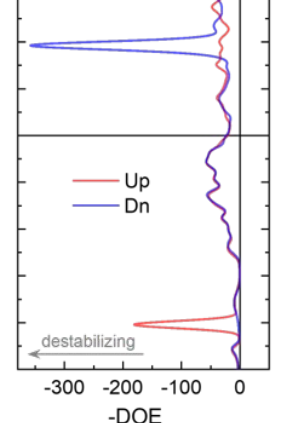
The observation of FSN validated by the LRF confirms the presence of electron instability in  $GdRu_2X_2$ . This argument is further examined by calculating the DOE. The DOE accounts for both interatomic and on-site atomic energy contributions as it integrates the entire electronic band structure with respect to energy (Eq (2)), unlike COHP, which focuses only on interatomic (pair-wise) interactions. Figure 9 shows the DOEs and the corresponding integrals. Overall, there are strongly destabilizing energy contributions (negative -DOE values), consistent with the electron instability underpinning FSN. The integrated DOE-band energy ( $E_{band}$ ) for  $GdRu_2X_2$  reveals that the chemical substitution of Si by Ge and Sn, separately, increases the overall destabilizing energy (**Figure 9**), as suggested by the Ru-Ru and Ru-X COHP curves (**Figure 3**). The  $E_{band}$  curves of  $GdRu_2X_2$  display similar shapes, confirming their resemblance in chemical and crystal structures.

$$E_{\text{band}} = \int_{-\infty}^{E_F} \text{DOE}(E) dE \tag{2}$$



Open Access Article. Published on 22 Oktoba 2025. Downloaded on 17/11/2025 22:02:13.





 $GdRu_2Sn_2$ 

d

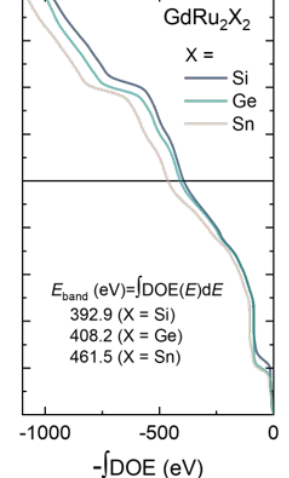


**Figure 9**. Density of energy analysis of (a)  $GdRu_2Si_2$ , (b)  $GdRu_2Ge_2$ , and (c)  $GdRu_2Sn_2$ . (d) Comparison of band energy ( $E_{band}$ ) for  $GdRu_2X_2$  where X = Si, Ge and Sn).

# 4. Exchange Interaction Evaluation

In addition to the bonding and DOE analysis, we study the exchange interactions in  $GdRu_2X_2$ . Building upon our earlier findings, <sup>41</sup> here we performed an energy-mapping analysis, using DFT calculations, as illustrated in **Figure 10**. <sup>62,71-73</sup> The Gd spins form two square sublattices within a unit cell. Our model incorporates the nearest-neighbor exchange interaction  $J_1$  along the a- or b-axis, the exchange interaction  $J_2$  between the Gd square sublattices and the interaction  $J_3$  within the ab-plane along the [110] direction. To accurately simulate an extended solid and avoid artificial interactions between periodic images of atoms, we used a (2a, 2b, c) supercell (containing four formula units) and six different spin-ordered states (**Figure 10**). The total spin exchange energy per supercell can be expressed by the following equations:<sup>5</sup>

$$E_{1} = E_{0} + (-8J_{1} + 0J_{3} + 0J_{2}) \cdot S^{2}$$

$$E_{2} = E_{0} + (0J_{1} - 16J_{3} + 0J_{2}) \cdot S^{2}$$

$$E_{3} = E_{0} + (0J_{1} + 0J_{3} - 8J_{2}) \cdot S^{2}$$

$$E_{4} = E_{0} + (8J_{1} - 8J_{3} + 0J_{2}) \cdot S^{2}$$

$$E_{5} = E_{0} + (8J_{1} + 0J_{3} + 0J_{2}) \cdot S^{2}$$

$$E_{6} = E_{0} + (16J_{1} - 16J_{3} + 0J_{2}) \cdot S^{2}$$
(3)

where the  $E_0$  corresponds to the non-magnetic contribution to the total energy, and S = 7/2, the spin for  $Gd^{3+}$ . From these energies, the exchange interactions per four formula units can be calculated as:

$$J_1 = \frac{(E_6 - E_2)}{16S^2}$$

$$J_2 = \frac{(E_1 + E_5 - 2E_3)}{16S^2}$$
(4)

Open Access Article. Published on 22 Oktoba 2025. Downloaded on 17/11/2025 22:02:13.

$$J_3 = \frac{(E_5 - E_4)}{8S^2}$$

The *J*-coupling interaction can then be obtained:

**Table 1**. Calculated *J*-coupling constants and an inverse of the Mean Absolute Deviation  $(MAD^{-1})$  for  $GdRu_2X_2$  (X = Si, Ge, Sn)

X Site	<i>J</i> <sub>1</sub>  (K)	J <sub>2</sub>   (K)	J <sub>3</sub>   (K)	MAD <sup>-1</sup>
Si	0.7(2)	153.5(2)	0.5(2)	0.015
Ge	71.1(2)	153.8(2)	2.3(2)	0.019
Sn	76.2(2)	153.0(2)	0.3(2)	0.020

As shown in **Table 1**,  $J_1$  varies from negligible to strong ferromagnetic (FM) when the X site changes from Si to Sn. Meanwhile,  $J_2$  remains unaffected by the X site, which reveals that the shape of the Gd orbitals changes primarily along the a or b axis when Si is replaced by Ge/Sn, suggesting an enhancement of  $J_1$ .

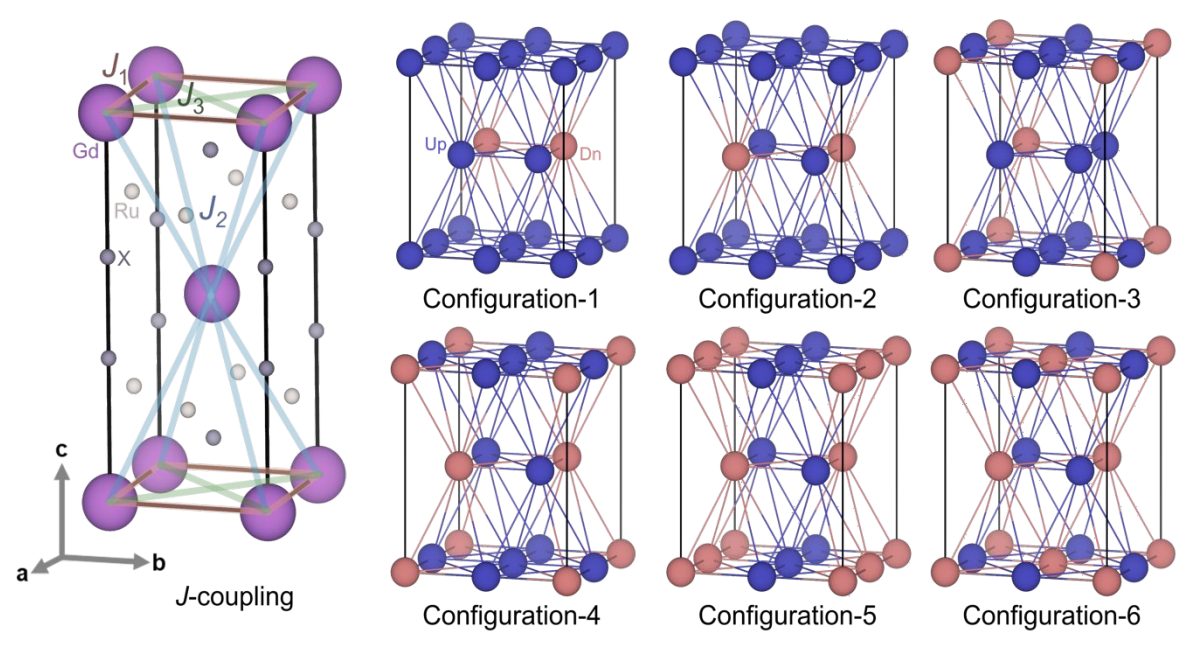


**Figure 10.** Representing exchange interactions  $J_1$ ,  $J_2$  and  $J_3$  between  $Gd^{3+}$  atoms within the unit cell and spin-ordered states within the (2a, 2b, c) supercell based on energy mapping method. Pink and blue colors correspond to the spin down and up, respectively.



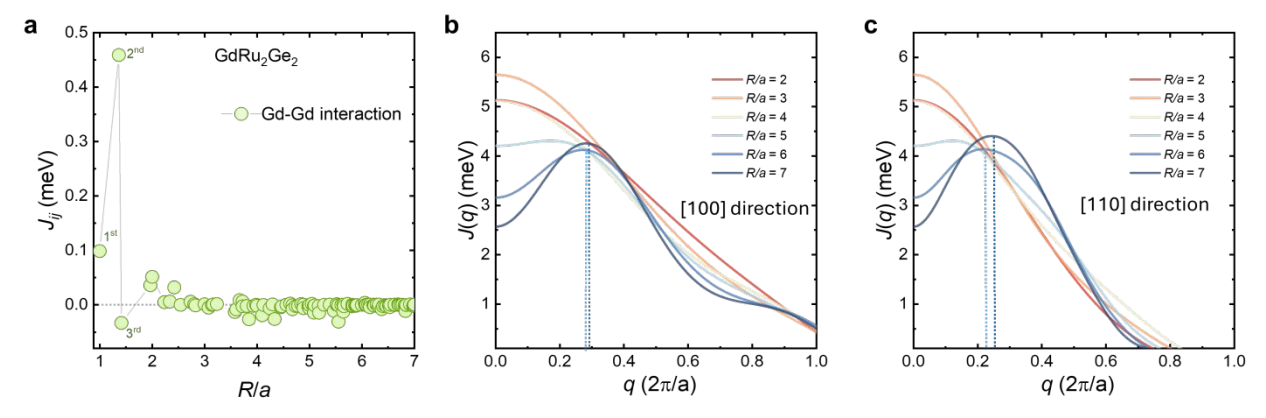


Figure 11. Exchange interaction calculations based on magnetic force theorem (a) Gd-Gd exchange interactions as a function of reciprocal lattice distance  $I_{ii}(R)$ , R - lattice translational vector, a lattice constant and (R/a) - Cluster radius, (b) and (c) Reciprocal space exchange interaction function I(q) along [100] and [110] directions respectively.

To assess the competing strength of these exchange interactions, we calculated the inverse of the Mean Absolute Deviation (MAD<sup>-1</sup>), which measures the closeness of interaction strengths. As the X site progresses from Si to Ge and Sn, the MAD<sup>-1</sup> value improves from 0.015 to 0.019 and 0.020, respectively. This increase in the appreciable, competing FM and AFM interactions in the Gd square lattice (the ab-plane) as a function of X follows similar trends in enhanced electronic instability and destabilizing energy  $E_{\rm band}$ . Competing FM and AFM interactions bear a resemblance to those in other skyrmion hosts.

For further insight into long-range RKKY exchange interactions within GdRu<sub>2</sub>Ge<sub>2</sub>, additional exchange interaction calculations were performed based on the magnetic force theorem using the LKAG scheme. Magnetic exchange constants  $(J_{ij})$  between Gd moments as a function of scaled distance (R/a) are shown in **Figure 11(a)**. We observed predominantly FM interactions (positive  $J_{ij}$ ) for (R/a) < 2; however, oscillatory behavior is seen up to (R/a) = 7, indicating long-range RKKY interaction. The strongest interaction is identified as the second-neighbor (interlayer) coupling  $I_2$ , corresponding to the body-diagonal direction [111]. Since  $J_8$  ((R/a) = c) also shows a strong ferromagnetic interaction, the interplane exchange  $(J_2, J_8)$  is stronger than the basal-plane interactions  $J_1$  and  $J_3$ . The competition between intra- and interlayer exchange frustration suggests the presence of non-collinear magnetic ordering in GdRu<sub>2</sub>Ge<sub>2</sub>. To examine whether the system has spin density wave modulation, we performed a lattice Fourier transform of the real-space exchange constants and estimated I(q), with q expressed in units of  $2\pi/a$  (**Figure 11b**). For cluster radii smaller than 4, FM interaction is stabilized, but above this radius we observed a stable peak with an amplitude of about 4 meV, located at  $\mathbf{Q}_A = (0.3, 0, 0)$  r.l.u. along  $\Gamma$ -X direction. This SDW

Open Access Article. Published on 22 Oktoba 2025. Downloaded on 17/11/2025 22:02:13.

modulation was observed experimentally in both GdRu<sub>2</sub>Ge<sub>2</sub> and GdRu<sub>2</sub>Si<sub>2</sub>.41,48,74 The Fourier transform of  $J_{ij}$  along the  $\Gamma$ -M direction [110] also shows a peak at  $\mathbf{Q}_B = (0.25, 0.25, 0)$  r.l.u. with an amplitude of 4.5 meV, indicating that the system favors a multi-Q state where the modulations along [100] and [110] coexist (**Figure 11 b and c**).

We propose a correlation between  $E_{\text{band}}$  and the temperature and magnetic field conditions at which skyrmions emerge (Figure 12). For the Si and Ge materials, the conditions for skyrmion formation have been experimentally proven. Our attempts to create the Sn version have not been fruitful yet, possibly due to its highest electron instability and thermodynamically unfavorable formation energy among the series. GdRu<sub>2</sub>Sn<sub>2</sub> exhibits 72 meV/atom above the convex hull and is predicted to decompose into GdSn<sub>2</sub> + 2Ru (**Figure S1b**). Unconventional synthesis approaches, such as ion exchange or high-pressure synthesis, may be required to access this metastable phase. While we are making additional efforts to create GdRu<sub>2</sub>Sn<sub>2</sub>, we predict that this phase hosts skyrmions at a higher temperature and a lower field than its siblings, attributable to its highest destabilizing energy  $E_{\text{band}}$ . This prediction can be justified by the DOE formalism, which fundamentally paints the entire energetic picture.

Taken together, we propose a trend: the more destabilizing energy  $E_{\text{band}}$  and the more competing FM and AFM interactions in the Gd square lattice, the more accessible skyrmion formation becomes (higher temperatures and lower fields) (Figure 12). This suggestion demonstrates that destabilizing energy contributions and competing interaction strengths can serve as indicators for predicting and realizing the emergence of skyrmions. While the suggested trend may prove useful, it warrants rigorous experimental evidence for the Sn material.

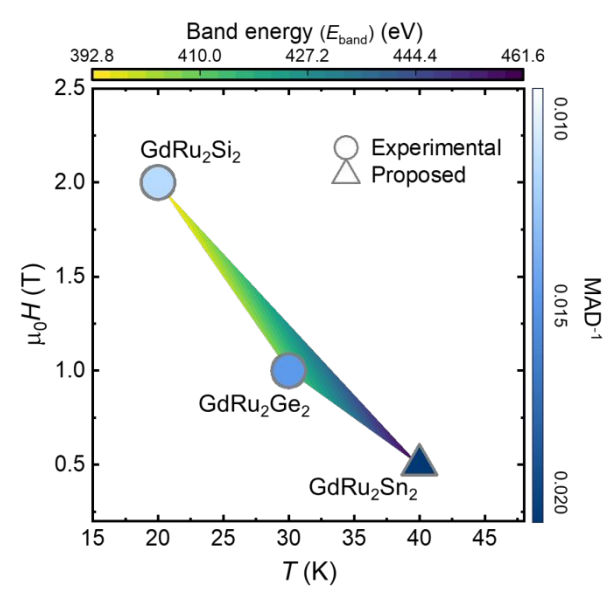


**Figure 12.** Correlation between skyrmion formation T, and  $\mu_0 H$  with band energy ( $E_{band}$ ) for  $GdRu_2X_2$  (X = Si, Ge, and Sn), with the blue color filling indicate the MAD<sup>-1</sup>.

#### **CONCLUSIONS**

Developing skyrmion materials for spintronics requires a comprehensive understanding of the chemical origins that facilitate a system undergoing a phase transition under a given condition to form topologically distinct spin phases. Our results provide a new pathway toward understanding and developing centrosymmetric magnetic metals that host skyrmions, rooted in chemical concepts in solids. We study the impact of X-p (Si-3p/Ge-4p/Sn-5p) orbitals on the skyrmion evolution in GdRu<sub>2</sub>X<sub>2</sub>. chemical bonding analysis reveals that increased interactions occur between the

Gd-4f localized electrons and the [Ru<sub>2</sub>X<sub>2</sub>] conduction layer as X changes from Si-3p to Ge-4p and Sn-5p (resulting in more extended orbitals). The realization of FSN indicates the electron instability in  $GdRu_2X_2$ . In this analysis, an FSN vector [ $\mathbf{Q}_A = (q, 0, 0)$ ] r.l.u. and two inequivalent FSN vectors  $[\mathbf{Q}_A = (q, 0, 0); \mathbf{Q}_B = (q, q, 0)]$  r.l.u. are extracted for the Si and Ge compounds, respectively. For the Sn material, multiple FSN vectors are suggested. The competition between RKKY interactions at different wavevectors, stemming from FSN along several directions, can work in favor of skyrmion formation in centrosymmetric magnetic metals. The DOE analysis complements COHP in that it captures the significance of both interatomic and atomic energetic contributions for electron (in)stability. We propose that the more destabilizing energy and the stronger competing interaction, the more accessible conditions are for skyrmions to emerge (at higher temperatures and lower fields). Ongoing experimental studies on the Sn compound will help verify this proposed trend. Overall, our work provides a new framework for approaching skyrmion materials research from chemical bonding and electronic instability perspectives, while inviting other studies to dissect the multifaceted aspects of the emergence of topologically nontrivial states of matter for high-density memory and logic architectures.

# ASSOCIATED CONTENT

# Abbreviations.

RKKY - Ruderman-Kittel-Kasuya-Yosida (exchange interaction)

Open Access Article. Published on 22 Oktoba 2025. Downloaded on 17/11/2025 22:02:13.

FSN – Fermi surface nesting

DFT – Density Functional Theory

GGA – Generalized Gradient Approximation

PAW - Projector Augmented Wave

LCAO – Linear Combination of Atomic Orbitals

LOBSTER - Local Orbital Basis Suite Towards Electronic-Structure Reconstruction

COHP - Crystal Orbital Hamilton Population

*k*-COHP – k-space resolved Crystal Orbital Hamilton Population

COBI - Crystal Orbital Bond Index

ICOHP – Integrated Crystal Orbital Hamilton Population

ICOBI - Integrated Crystal Orbital Bond Index

MO - Molecular Orbital

DOE – Density of Energy

LRF – Lindhard Response Function

FS – Fermi Surface

FM / AFM – Ferromagnetic / Antiferromagnetic

MAD - Mean Absolute Deviation

**Supporting Information**. Additional data analysis, tables, figures, including COBI, Fermi surface. This material is available free of charge via the Internet at http://pubs.acs.org.

#### **AUTHOR INFORMATION**

# **Corresponding Author**

\*Thao T. Tran, email: thao@clemson.edu.

#### **Author Contributions**

The manuscript was written through the contributions of all authors. All authors have given approval to the final version of the manuscript.

#### ACKNOWLEDGMENTS

The work at Clemson University was supported by the National Science Foundation under CAREER Award NSF-DMR-2338014. X.H. and R.K. thank the Arnold and Mabel Beckman Foundation for a 2023 BYI award to T.T.T. We acknowledge support from the Arnold and Mabel Beckman Foundation and the Camille and Henry Dreyfus Foundation. Research performed at Gdansk Tech was supported by the National Science Center (Poland) OPUS grant no. UMO-2022/45/B/ST5/03916. S.T. acknowledges support from ONR-N000142312061. We acknowledge the technical support from Peter C. Müller with the LOPOSTER code for *k*-space COHP data visualization. JS and CJB acknowledge the Minnesota Supercomputing Institute (MSI) at the University of Minnesota for providing resources that contributed to the research results reported within this paper. We thank the reviewers, especially reviewers #2 and #3, for their valuable insights.

#### **References:**

- Gui, X., Klein, R. A., Brown, C. M. & Xie, W. Chemical Bonding Governs Complex Magnetism in MnPt₅P. *Inorganic Chemistry* **60**, 87-96 (2020).
- Berry, T. *et al.* Bonding and Suppression of a Magnetic Phase Transition in EuMn<sub>2</sub>P<sub>2</sub>. *Journal of the American Chemical Society* **145**, 4527-4533 (2023).
- Amtry, S. M. *et al.* Chemical Design of Spin Frustration to Realize Topological Spin Glasses. *Journal of the American Chemical Society* (2024).
- 4 Pollak, C. J. et al. Chemical Bonding Induces One-Dimensional Physics in Bulk Crystal Bilr₄Se<sub>8</sub>. Journal of the American Chemical Society **146**, 6784-6795 (2024).
- Huai, X. *et al.* Noncentrosymmetric Triangular Magnet CaMnTeO<sub>6</sub>: Strong Quantum Fluctuations and Role of s<sup>0</sup> versus s<sup>2</sup> Electronic States in Competing Exchange Interactions. *Advanced Materials* **36**, 2313763 (2024).
- 6 Shumilov, K. D., Jenkins, A. J., La Pierre, H. S., Vlaisavljevich, B. & Li, X. Overdestabilization vs. Overstabilization in the Theoretical Analysis of *f*-Orbital Covalency. *Journal of the American Chemical Society* **146**, 12030-12039 (2024).
- 7 Li, H. *et al.* Discovery of conjoined charge density waves in the kagome superconductor CsV<sub>3</sub>Sb<sub>5</sub>. *Nature communications* **13**, 6348 (2022).
- Zhang, B., Tan, H., Yan, B., Xu, C. & Xiang, H. Atomistic Origin of Diverse Charge Density Wave States in CsV<sub>3</sub>Sb<sub>5</sub>. *Physical review letters* **132**, 096101 (2024).
- 9 Kurtulus, Y., Gilleßen, M. & Dronskowski, R. Electronic structure, chemical bonding, and finite-temperature magnetic properties of full Heusler alloys. *Journal of computational chemistry* **27**, 90-102 (2006).
- Yu, M. *et al.* Tunable eg orbital occupancy in Heusler compounds for oxygen evolution reaction. *Angewandte Chemie International Edition* **60**, 5800-5805 (2021).
- Neubauer, A. *et al.* Topological Hall effect in the A phase of MnSi. *Physical review letters* **102**, 186602 (2009).
- Zhang, X. et al. Skyrmion-electronics: writing, deleting, reading and processing magnetic skyrmions toward spintronic applications. *Journal of Physics: Condensed Matter* 32, 143001 (2020).
- Tokura, Y. & Kanazawa, N. Magnetic skyrmion materials. *Chemical Reviews* **121**, 2857-2897 (2020).
- Roychowdhury, S. *et al.* Giant Room-Temperature Topological Hall Effect in a Square-Net Ferromagnet LaMn2Ge2. *Advanced Materials* **36**, 2305916 (2024).
- 15 Chen, B. *et al.* Spintronic devices for high-density memory and neuromorphic computing—A review. *Materials Today* **70** (2023).
- 16 Pfleiderer, C. & Rosch, A. Single skyrmions spotted. *Nature* **465**, 880-881 (2010).
- Tang, N. *et al.* Skyrmion-Excited Spin-Wave Fractal Networks. *Advanced Materials* **35**, 2300416 (2023).
- 18 Felser, C. Skyrmions. *Angewandte chemie international edition* **52** (2013).
- 19 Wang, K., Bheemarasetty, V., Duan, J., Zhou, S. & Xiao, G. Fundamental physics and applications of skyrmions: A review. *Journal of Magnetism and Magnetic Materials* **563**, 169905 (2022).
- Kumar, N., Guin, S. N., Manna, K., Shekhar, C. & Felser, C. Topological quantum materials from the viewpoint of chemistry. *Chemical Reviews* **121**, 2780-2815 (2020).
- 21 Parkin, S. & Yang, S.-H. Memory on the racetrack. *Nature nanotechnology* **10**, 195-198 (2015).

Open Access Article. Published on 22 Oktoba 2025. Downloaded on 17/11/2025 22:02:13.

- Oyeka, E. E. *et al.* Potential skyrmion host Fe(IO<sub>3</sub>)<sub>3</sub>: connecting stereoactive lone-pair electron effects to the Dzyaloshinskii-Moriya interaction. *Chemistry of Materials* **33**, 4661-4671 (2021).
- 24 Kanazawa, N., Seki, S. & Tokura, Y. Noncentrosymmetric magnets hosting magnetic skyrmions. *Advanced Materials* **29**, 1603227 (2017).
- Zhang, C. *et al.* Above-room-temperature chiral skyrmion lattice and Dzyaloshinskii–Moriya interaction in a van der Waals ferromagnet Fe<sub>3-x</sub>GaTe<sub>2</sub>. *Nature Communications* **15**, 4472 (2024).
- Zhang, Y. *et al.* Stable skyrmion bundles at room temperature and zero magnetic field in a chiral magnet. *Nature Communications* **15**, 3391 (2024).
- 27 Singh, D. *et al.* Transition between distinct hybrid skyrmion textures through their hexagonal-to-square crystal transformation in a polar magnet. *Nature Communications* **14**, 8050 (2023).
- 28 Kézsmárki, I. *et al.* Néel-type skyrmion lattice with confined orientation in the polar magnetic semiconductor GaV<sub>4</sub>S<sub>8</sub>. *Nature materials* **14**, 1116-1122 (2015).
- 29 Chacon, A. *et al.* Observation of two independent skyrmion phases in a chiral magnetic material. *Nature physics* **14**, 936-941 (2018).
- 30 Mühlbauer, S. et al. Skyrmion lattice in a chiral magnet. Science 323, 915-919 (2009).
- Adams, T. *et al.* Long-wavelength helimagnetic order and skyrmion lattice phase in Cu<sub>2</sub>OSeO<sub>3</sub>. *Physical review letters* **108**, 237204 (2012).
- Kurumaji, T. *et al.* Néel-type skyrmion lattice in the tetragonal polar magnet VOSe<sub>2</sub>O<sub>5</sub>. *Physical review letters* **119**, 237201 (2017).
- Casas, B. W. *et al.* Coexistence of merons with skyrmions in the centrosymmetric van der Waals ferromagnet Fe5–xGeTe2. *Advanced Materials* **35**, 2212087 (2023).
- Kim, D.-H. *et al.* Bulk Dzyaloshinskii–Moriya interaction in amorphous ferrimagnetic alloys. *Nature materials* **18**, 685-690 (2019).
- Ishiwata, S. *et al.* Emergent topological spin structures in the centrosymmetric cubic perovskite SrFeO<sub>3</sub>. *Physical Review B* **101**, 134406 (2020).
- Kurumaji, T. *et al.* Skyrmion lattice with a giant topological Hall effect in a frustrated triangular-lattice magnet. *Science* **365**, 914-918 (2019).
- Moya, J. M. *et al.* Incommensurate magnetic orders and topological Hall effect in the square-net centrosymmetric EuGa<sub>2</sub>Al<sub>2</sub> system. *Physical Review Materials* **6**, 074201 (2022).
- Yasui, Y. *et al.* Imaging the coupling between itinerant electrons and localised moments in the centrosymmetric skyrmion magnet GdRu<sub>2</sub>Si<sub>2</sub>. *Nature communications* **11**, 5925 (2020).
- Zhou, Y., Li, S., Liang, X. & Zhou, Y. Topological spin textures: Basic physics and devices. *Advanced Materials* **37**, 2312935 (2025).
- 40 Yoshimochi, H. *et al.* Multistep topological transitions among meron and skyrmion crystals in a centrosymmetric magnet. *Nature Physics* **20**, 1-8 (2024).
- Dasuni N Rathnaweera, X. H., K. Ramesh Kumar, Michał J. Winiarski, Tomasz Klimczuk, and Thao T. Tran,. Atomically Modulating Competing Exchange Interactions in Centrosymmetric Skyrmion Hosts  $GdRu_2X_2$  (X = Si, Ge). <u>https://arxiv.org/abs/2502.21169</u> (2025).
- 42 Khanh, N. D. *et al.* Nanometric square skyrmion lattice in a centrosymmetric tetragonal magnet. *Nature Nanotechnology* **15**, 444-449 (2020).
- Gries, L. *et al.* Uniaxial pressure effects, phase diagram, and tricritical point in the centrosymmetric skyrmion lattice magnet GdRu 2 Si 2. *Physical Review B* **111**, 064419 (2025).
- Gupta, S. *et al.* Skyrmion phase in polycrystalline GdRu₂Si₂ revealed by magnetic susceptibility, topological Hall effect, and Shubnikov–de Haas-like quantum oscillations. *Physical Review B* **111**, 144405 (2025).

- Nomoto, T., Koretsune, T. & Arita, R. Formation mechanism of the helical **Q** structure in Gd-based skyrmion materials. *Physical Review Letters* **125**, 117204 (2020).
- Nomoto, T. & Arita, R. Ab initio exploration of short-pitch skyrmion materials: Role of orbital frustration. *Journal of Applied Physics* **133** (2023).
- Siebeneichler, S., Ovchinnikov, A., Sheptyakov, D. & Mudring, A.-V. Making a Hedgehog Spin-Vortex State Possible: Geometric Frustration on a Square Lattice. *Chemistry of Materials* **36**, 3546-3554 (2024).
- Wood, G. D. A. *et al.* Double-Q ground state with topological charge stripes in the centrosymmetric skyrmion candidate GdRu<sub>2</sub>Si<sub>2</sub>. *Physical Review B* **107**, L180402 (2023).
- Khanh, N. D. *et al.* Zoology of Multiple-Q Spin Textures in a Centrosymmetric Tetragonal Magnet with Itinerant Electrons. *Advanced Science* **9**, 2105452 (2022).
- Matsuyama, N. *et al.* Quantum oscillations in the centrosymmetric skyrmion-hosting magnet GdRu<sub>2</sub>Si<sub>2</sub>. *Physical Review B* **107**, 104421 (2023).
- Eremeev, S. V. *et al.* Insight into the electronic structure of the centrosymmetric skyrmion magnet GdRu<sub>2</sub>Si<sub>2</sub>. *Nanoscale Advances* **5**, 6678-6687 (2023).
- Maintz, S., Deringer, V. L., Tchougréeff, A. L. & Dronskowski, R. LOBSTER: A tool to extract chemical bonding from plane-wave based DFT. *Journal of Computational Chemistry* **37**, 1030-1035 (2016).
- Deringer, V. L., Tchougréeff, A. L. & Dronskowski, R. Crystal orbital Hamilton population (COHP) analysis as projected from plane-wave basis sets. *The journal of physical chemistry A* **115**, 5461-5466 (2011).
- Sun, X. et al. Achieving band convergence by tuning the bonding ionicity in n-type Mg<sub>3</sub>Sb<sub>2</sub>. Journal of computational chemistry **40**, 1693-1700 (2019).
- Müller, P. C., Ertural, C., Hempelmann, J. & Dronskowski, R. Crystal orbital bond index: Covalent bond orders in solids. *The Journal of Physical Chemistry C* **125**, 7959-7970 (2021).
- Küpers, M. et al. Unexpected Ge–Ge contacts in the two-dimensional Ge₄Se₃Te Phase and analysis of their chemical cause with the density of energy (DOE) function. Angewandte Chemie International Edition **56**, 10204-10208 (2017).
- Wang, Y., Müller, P. C., Hemker, D. & Dronskowski, R. LOPOSTER: A Cascading Postprocessor for LOBSTER. *Journal of Computational Chemistry* **46**, e70167 (2025).
- Kawamura, M. FermiSurfer: Fermi-surface viewer providing multiple representation schemes. *Computer Physics Communications* **239**, 197-203 (2019).
- Ebert, H., Koedderitzsch, D. & Minar, J. Calculating condensed matter properties using the KKR-Green's function method—recent developments and applications. *Reports on Progress in Physics* **74**, 096501 (2011).
- Vosko, S. H., Wilk, L. & Nusair, M. Accurate spin-dependent electron liquid correlation energies for local spin density calculations: a critical analysis. *Canadian Journal of physics* **58**, 1200-1211 (1980).
- Liechtenstein, A. I., Katsnelson, M., Antropov, V. & Gubanov, V. Local spin density functional approach to the theory of exchange interactions in ferromagnetic metals and alloys. *Journal of Magnetism and Magnetic Materials* **67**, 65-74 (1987).
- 62 Giannozzi, P. et al. QUANTUM ESPRESSO: a modular and open-source software project for quantum simulations of materials. *Journal of physics: Condensed matter* **21**, 395502 (2009).
- 63 Maintz, S., Deringer, V. L., Tchougréeff, A. L. & Dronskowski, R. (Wiley Online Library, 2016).
- Nelson, R. *et al.* LOBSTER: Local orbital projections, atomic charges, and chemical-bonding analysis from projector-augmented-wave-based density-functional theory. *Journal of Computational Chemistry* **41**, 1931-1940 (2020).

- Dronskowski, R. & Blöchl, P. E. Crystal orbital Hamilton populations (COHP): energy-resolved visualization of chemical bonding in solids based on density-functional calculations. *The Journal of Physical Chemistry* **97**, 8617-8624 (1993).
- Maintz, S., Deringer, V. L., Tchougréeff, A. L. & Dronskowski, R. Analytic projection from plane-wave and PAW wavefunctions and application to chemical-bonding analysis in solids. *Journal of computational chemistry* **34**, 2557-2567 (2013).
- Dronskowski, R. *Computational chemistry of solid state materials: a guide for materials scientists, chemists, physicists and others*. Vol. 146 (John Wiley & Sons, 2008).
- Muller, P. C., Reitz, L. S., Hemker, D. & Dronskowski, R. Orbital-Based Bonding Analysis in Solids. *Chemical Science* (2025). https://doi.org/10.1039/D5SC02936H
- Müller, P. C., Schmit, N., Sann, L., Steinberg, S. & Dronskowski, R. Fragment Orbitals Extracted from First-Principles Plane-Wave Calculations. *Inorganic Chemistry* **63** (2024).
- Landrum, G. A., Dronskowski, R., Niewa, R. & DiSalvo, F. J. Electronic structure and bonding in cerium (nitride) compounds: Trivalent versus tetravalent cerium. *Chemistry–A European Journal* **5**, 515-522 (1999).
- Whangbo, M.-H., Koo, H.-J. & Dai, D. Spin exchange interactions and magnetic structures of extended magnetic solids with localized spins: theoretical descriptions on formal, quantitative and qualitative levels. *Journal of Solid State Chemistry* **176**, 417-481 (2003).
- Xiang, H., Lee, C., Koo, H.-J., Gong, X. & Whangbo, M.-H. Magnetic properties and energy-mapping analysis. *Dalton Transactions* **42**, 823-853 (2013).
- Zvereva, E. A. *et al.* Hidden magnetic order in the triangular-lattice magnet Li<sub>2</sub>MnTeO<sub>6</sub>. *Physical Review B* **102**, 094433 (2020).
- Sarkar, S. *et al.* Unveiling Mysteries of GdRu<sub>2</sub>Si<sub>2</sub>: 3D Magnetism in a layered like Magnet. *arXiv* preprint arXiv:2409.06736 (2024).

The data supporting this article have been included as part of the Supplementary Information.